ARMA 19–1957

Geometric and Fractal Analysis of Complex Wormholes Resulting from Gypsum Core Flood Tests

Li, W.
Massachusetts Institute of Technology, Cambridge, MA, USA
Einstein, H. H.
Massachusetts Institute of Technology, Cambridge, MA, USA
Germaine, J. T.
Tufts University, Medford, MA, USA

Copyright 2019 ARMA, American Rock Mechanics Association

This paper was prepared for presentation at the 53rd US Rock Mechanics/Geomechanics Symposium held in New York, NY, USA, 23–26 June 2019. This paper was selected for presentation at the symposium by an ARMA Technical Program Committee based on a technical and critical review of the paper by a minimum of two technical reviewers. The material, as presented, does not necessarily reflect any position of ARMA, its officers, or members. Electronic reproduction, distribution, or storage of any part of this paper for commercial purposes without the written consent of ARMA is prohibited. Permission to reproduce in print is restricted to an abstract of not more than 200 words; illustrations may not be copied. The abstract must contain conspicuous acknowledgement of where and by whom the paper was presented.

ABSTRACT: Wormholes are long, finger-like channels that form due to the flow and dissolution heterogeneity in the soluble porous rock matrix. Wormholes are major flow pathways, which significantly increase the permeability of the rock formation. A fundamental understanding of the wormhole formation is crucial in civil, environmental and energy engineering research and practice. A series of gypsum core flood tests were conducted to study the effect of flow rate on the dissolution of the gypsum rock matrix and the formation of wormholes. High-resolution X-Ray computed tomography (CT) was used to determine the geometry of the wormholes resulting from different flow rates. Skeleton analysis and fractal analysis were used to study the geometry of the wormholes resulting from different flow rates using skeleton analysis and fractal analysis. These analyses showed that higher flow rates resulted in more complex wormholes regarding the total wormhole length and fractal dimensions.

1. INTRODUCTION

In an underground rock-fluid system, wormhole formation is a process resulting from flow and dissolution heterogeneity. Wormhole formation is common during underground reactive transport processes such as gypsum karst, limestone karst, acid stimulation and CO_2 sequestration. The reactive transport processes in the underground rock-fluid system involve two coupled processes: reactions (for example, dissolution) and fluid flow (flow in the porous matrix and fractures) driving the evolution of the rock-fluid systems. The formation of wormholes is a favorable process in oil reservoir acid stimulation, as it increases the reservoir permeability and thus oil production. However, it could also be an undesired process from the civil engineering perspective when the wormholes further develop into larger caverns, sinkholes and ground subsidence (Li et al., 2019). It is therefore essential to have a better knowledge of the factors that influence the formation of wormholes.

There have been many experimental studies to investigate the effect of flow rate on wormhole formation (Daccord, 1987; Daccord and Lenormand, 1987; Hoefner and Fogler, 1988; Daccord et al.,1993a,b; Taylor et al., 2002; Noiriel et al., 2009; Gomaa et al., 2010; El-Maghraby and Blunt, 2012; Sayed et al., 2012; Smith et al., 2013; Hao et al., 2013; Mohamed et al., 2013; Smith et al., 2014; Reynolds et al., 2014; Ghommem et al., 2015; Menke et al., 2016; Wang et al., 2016; Noiriel and Daval, 2017; Smith et al., 2017; Cai et al., 2018; Lin et al., 2016; Al-Khulaifi et al., 2018; Menke et al., 2018). In these experiments, core flood tests have been used extensively because of their versatility in controlling and monitoring the confining stress, deviatoric stress, inlet pressure, outlet pressure and specimen deformation during the tests. Some researchers used X-ray computed tomography (CT) scans on the specimen before and after the test to study the change of pore space and the formation of the wormholes (Gouze et al., 2003; Noiriel et al., 2004; Noiriel, 2015; Deng et al., 2015, 2016, 2017). The X-ray CT scans showed the 3D geometry of the wormholes and provided a generally accepted conclusion that higher flow rates result in more complex wormholes. However, these CT analyses mainly focused on the statistical parameters of the pore space such as porosity, and pore size distribution. The descriptions of the wormholes so far

were mostly qualitative, making it difficult to compare the effect of flow rate on the formation of wormholes. One therefore needs to characterize the wormholes with quantitative parameters to compare the wormholes resulting from different flow rates.

The present paper builds on the experiments reported by Li et al. (2019) to study the rock matrix dissolution and wormhole formation in a gypsum-water system. 3D topological and morphological algorithms were introduced by Li et al. (2019) to study the wormhole geometry quantitatively based on the CT scan data. In this paper, we are now using 3D skeleton analysis and fractal analysis to further the quantitative understanding of wormhole formation resulting from different flow rates. The paper starts with an introduction on the material and experimental methods in Section 2. The CT scan data of the specimens before core flood tests are presented in Sections 3. In Section 4, 3D skeleton analysis and fractal analysis are introduced to provide a quantitative description on the complex wormhole geometries. These 3D analyses use parameters such as wormhole length and fractal dimensions to quantitatively compare the wormholes resulting from different flow rates. Section 5 summarizes the analysis results and insights gained from these analyses.

2. MATERIAL AND EXPERIMENTAL METHODS

For better understanding, this paper provides a brief introduction on the material and experimental methods. The reader is referred to the paper by Li et al. (2019) for details of material properties and experimental methods.

2.1. Specimen preparation and material properties

Gypsum is one of the most soluble common rocks. The dissolution of gypsum forms caves, sinkholes, disappearing streams, and other karst features that are also found in limestones and dolomites. Gypsum dissolution is particularly relevant since gypsum also has very low strength and dissolution may eventually lead to failure. In addition, the dissolution kinetics of the gypsum water system is similar to the limestone-acid system (Daccord, 1987), making it an analogous material for studying acid stimulation. In this study, laboratory cast Plaster of Paris was used to prepare gypsum specimens because of its consistency and workability, similar to Daccord's experiments. The plaster used was molding Plaster of Paris manufactured by the U.S. Gypsum company. More than 95% of the material is calcium sulfate hemihydrate ($CaSO4 \cdot ½H2O$), the rest are crystalline silica, limestone and dolomite (NO. 1 Moulding Plasters, 2017).

A PVC tube with 35.56 mm inner diameter and 89 mm length was used as a mold for the plaster cast. A mass ratio of 0.6 water to plaster was used, as used by Einstein et al., (1969), to produce good workability. The plaster and water were mixed in a mixer for two minutes, then poured into the mold and vibrated for another two minutes to achieve uniformity and reduce the air bubbles in the specimen. After the specimen was cured in a 40 $^{\circ}C$ oven for one day, the gypsum had enough strength to be unmolded. The 40 $^{\circ}C$ temperature was proposed by Einstein et al., (1969), to prevent the gypsum from dehydration. The specimen was further cured at 40 $^{\circ}C$ for seven days to achieve enough strength. The specimen was then cut and polished to 82.55 *mm* in length for the core flood test (Figure 1).

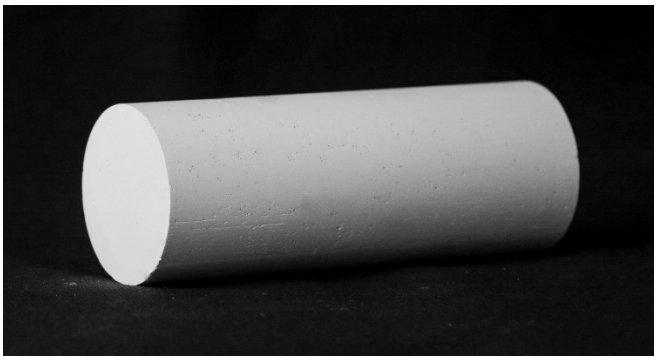

Figure 1. Gypsum specimen for core flood tests.

The specimen preparation method produced specimens with consistent key material properties such as porosity and initial hydraulic conductivity. The density of the specimen was around 1.216 g/cm^3, obtained by measuring the dimensions and the mass of the specimen. Assuming a specific gravity of 2.33 for the gypsum crystals (Serafeimidis and Anagnostou, 2013), the porosity calculated based on phase relations was in the range of 0.46-0.49. Mercury intrusion porosimetry (MIP) was also used to measure the porosity of the specimen. The porosity measured using MIP was 0.469, which was consistent with the porosity calculated based on phase relations. The MIP also showed that the pores at the scale of several microns contribute most of the porosity. In the core flood tests, the initial permeability of the material reflected the permeability of the gypsum matrix that had not been affected by the dissolution. The measured permeability of the material was in the range of 21 to 29 mD, which corresponds to a hydraulic conductivity of $2.06 - 2.85 \times 10^{-7}\ m/s$.

2.2. Experimental Setup

A computer-controlled triaxial system was used to apply confining pressure on the specimen and inject distilled water through the specimen. The computer-controlled triaxial system was designed and built in the MIT Geotechnical Engineering Laboratory with progressive updates over the past two decades by Sheahan and Germaine (1992); Andersen (1991); and Abdulhadi et al. (2011). This system was originally designed for

mechanical tests on soils and was updated for core flood tests by adding an outlet pressure transducer, upgrading the capacity of the water injection pressure-volume actuator (PVA; this is in essence a syringe pump), and integrating the effluent chemistry monitoring system (ECMS). Figure 2 is a diagram of this computer-controlled triaxial setup. The details of the original triaxial system were discussed in the paper by Sheahan and Germaine (1992). As shown in Figure 2, the specimen was mounted between the pedestal and ECMS top end cap with porous stones to spread the flow. The specimen was sealed with two membrane-sleeves between the pedestal and top end cap with three O-rings on each side. The confining pressure was applied with the cell oil using the cell PVA. The axial stress was applied through the top end cap by a load frame, which is not shown in Figure 2 for simplification.

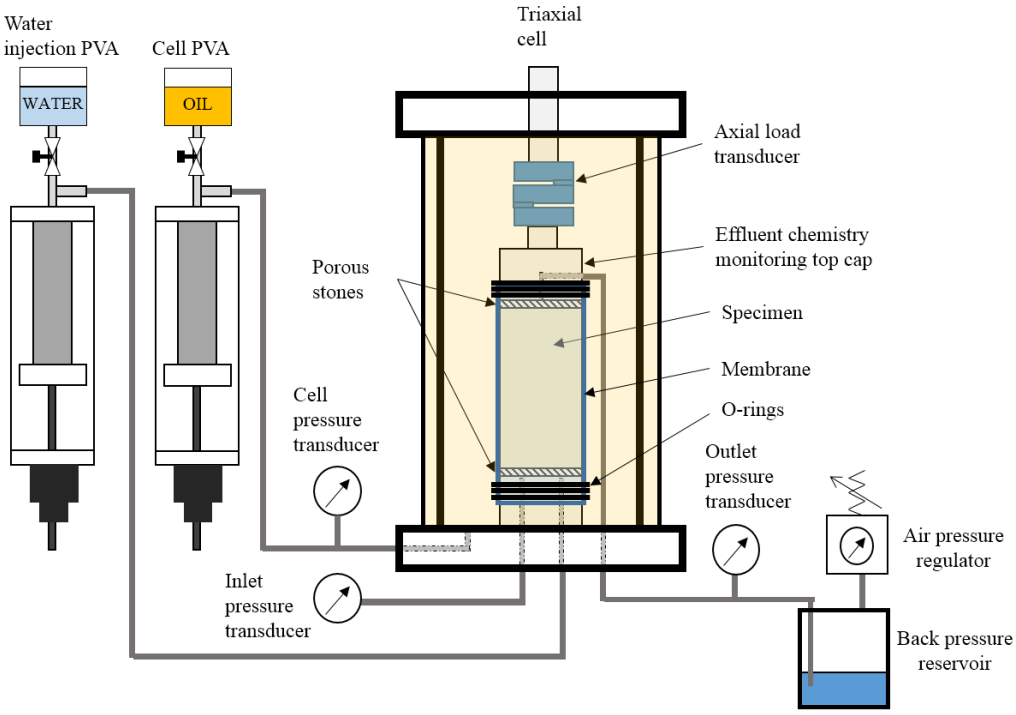

Figure 2 Diagram of the triaxial setup adapted for core flood tests. The parts in the setup are not drawn in the same scale.

2.3. *X-ray CT scan*

After the flow tests, the specimens were viewed with the CT scan using the MicroCT system at the Center of Nanoscale Systems at Harvard University. A digital image sensor with 2000×2000 pixels of size 200 μm was used to record each radiograph with a 16-bit precision (Figure 3(a)). The positioning of the specimen between the X-ray source and the image sensor yielded a 4× magnification, which resulted in radiographs of the specimen with a resolution of 50 μm (49.514 μm). The exposure time for each radiograph was 1 second. 1955 X-ray graphic projections (Figure 3(b)) were taken as the specimen rotates 360° to generate enough data for reconstructing the 3D model of the specimen.

The software Inspect-X 3D was used to reconstruct the 3D model of the specimen based on the 1955 radiographic projections. The 3D model was then exported as image stack of horizontal cross-sections of the specimen. Figure 3(c) shows two of the cross-sections of the specimen. Each image in the image stack is the greyscale cross section of the specimen, with higher brightness representing higher density and lower brightness representing lower density. Since the specimen material is almost pure gypsum, image segmentation for the solid phase and air phase is relatively straightforward (Deng et al., 2016). The global thresholding method was used to provide fast segmentation. On each binary cross-section, 1 (white) represents solid and 0 (black) represents void. Since the void space in the specimen is of main interest for the analysis, the binary cross-sections are inverted, using 1 (white) to represent the void space. The void space outside of the specimen is also set as 0, as shown in Figure 3(d). The inverted image stacks were then converted to a 3D binary matrix representing the entire specimen (Figure 3(e)). The location of each matrix element corresponds to the location of the voxel in the 3D model of the specimen. By using a binary matrix to represent the 3D specimen model, the amount of data can be reduced from several gigabytes to several megabytes for faster processing and analysis (Su et al., 2019).

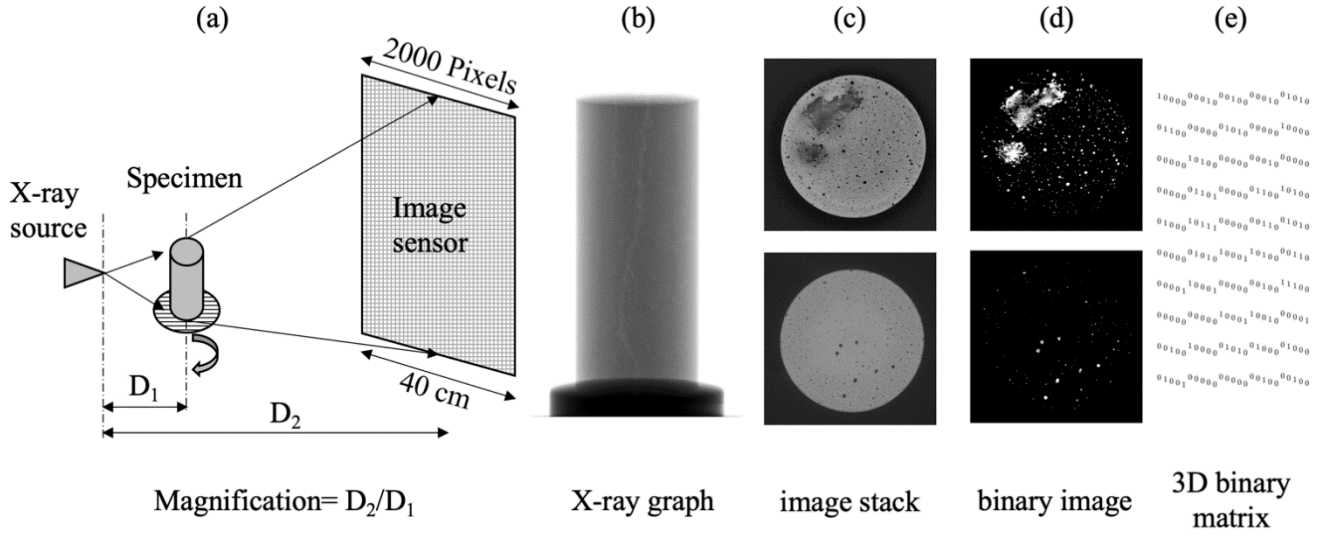

Figure 3. CT scan data acquisition and processing. (a) Schematic of the CT scan setup. (b) One of the 1955 radiographic projections. (c) Image stack of horizontal cross-sections of the specimen. (d) Binary image of the cross-sections with 1 (white) to represent the void space. (d) 3D binary matrix representing the specimen (only a 5×5×10 box of the matrix is used to demonstrate the 3D binary matrix).

2.4. Experimental processes

The core flood tests follow these experimental processes:

- measure specimen mass and dimensions;
- install the specimen and its membrane seals in the triaxial cell;
- apply 400 *kPa* uniform stress on the specimen;
- vacuum saturate specimen with fully-saturated gypsum solution;
- apply 70 *kPa* back pressure;
- saturate the specimen over one night for temperature equilibrium;
- flow about 500 mL distilled water through the specimen, during which the effluent concentration, pressures and injected volumes are measured;
- take out the specimen and dry in 40 ˚*C* oven;
- measure specimen mass and dimensions;
- X-ray CT scan.

Seven core flood tests were conducted to study the matrix dissolution and wormhole formation as a function of the injection flow rate. Each test used a gypsum specimen that was prepared according to the procedure described in Section 2.1. Each core flood test used one constant flow rate throughout the test. The seven flow rates used for the seven tests were logarithmically spaced as: 5.00, 7.07, 10.00, 14.14, 20.00, 28.28 and 40.00 $\mu L/s$.

3. INTIAL PORE SPACE ANALYSIS

Since the specimens prepared according to Section 2.1 had consistent material properties, only a single CT scan was conducted on one of the specimens before the core flood test. This CT scan result is assumed to be representative of the other specimens for initial pore space analysis. Since the CT scan had a resolution of 50 μm, it could only resolve pores larger than 50 μm. Although the pore space analysis based on the CT data is limited by its resolution, it is useful in the wormhole geometry analysis, in which the pores and wormholes need to be differentiated.

In the 3D binary matrix, a pore is represented by a cluster of connected elements with value 1. These connected elements can be identified by the MATLAB algorithm as "connected components". Therefore, each connected component is an individual pore, which consists of a certain number N_{vi} of voxels. Volume V_i and equivalent diameter D_i of each pore can be calculated based on N_{vi} using Equation (1) and Equation (2), respectively:

$$V_i = N_{vi} \times (50\ \mu m)^3, \tag{1}$$

$$D_i = \sqrt[3]{\frac{6V_i}{\pi}}, \tag{2}$$

To eliminate the noise of the CT image sensor for a reliable analysis, the 3D binary matrix representing the specimen before the test was filtered by an 8-voxel 3D filter. The 8-voxel 3D filter had equivalent diameters of 124.07 μm based on Equations (1) and (2). This initial

filter also deleted the pores that were represented by less than eight voxels in the CT scan. After applying the initial 3D filter, there were 97,330 pores left in the specimen that were larger than 124.07 μm. These pores were the small air bubbles trapped in the specimen during the specimen preparation processes. The total volume of these pores normalized by the volume of the specimen is the porosity 0.0092. This indicated that the porosity contributed by pores larger than 124.07 μm was 0.0092. These pores contributed a very small part of the overall porosity 0.469, since the major contribution is from pores at the scale of several microns, as discussed in Section 2.1. The specimen and the pores are reconstructed in Figure 4. The reconstructed pores are isolated from each other and distributed uniformly in the specimen, which does not provide a preferred flow path.

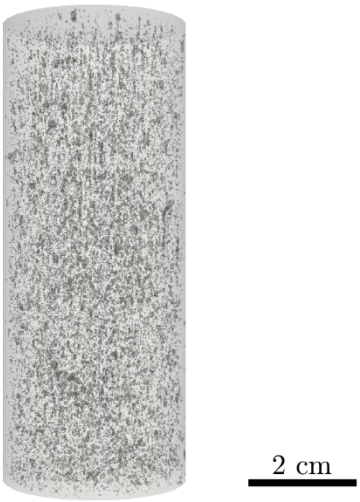

Figure 4. 3D reconstruction of initial pores larger than 124.07μm.

4. QUANTITATIVE WORMHOLE GEOMETRY ANALYSIS

4.1. 3D wormhole reconstruction

The 3D binary matrices representing the seven specimens after the core flood tests were used for the wormhole geometry analysis. First, 1000-voxel 3D filter was used to eliminate the isolated pores and reveal the wormholes formed in the specimen during the core flood tests. The 1000-voxel 3D filter, which had an equivalent diameter of 600 μm, eliminated most of the isolated pores. Another length filter was applied to eliminate pores that were shorter than 5mm in the axial direction of the specimen. This filter eliminated isolated pores that were not eliminated by the 1000-voxel 3D filter and the wormholes that were shorter than 5mm in the axial direction of the specimen. The 1000-voxel 3D filter and 5 *mm* length filter were chosen so that the isolated pores can be effectively eliminated, and the wormholes could be preserved. The 5 *mm* length filter also acted as a criterion for the wormhole geometry analysis so that only wormholes longer than 5 mm were accounted for.

After the filtering process discussed above, the 3D binary matrix was used to reconstruct the wormholes. The software ParaView® was used to produce the 3D rendering of the wormholes shown in Figure 5. The area of each wormhole projected on the horizontal plane was used to calculate the equivalent diameter of the wormhole, as indicated in color in Figure 5. The specimens were reconstructed in the same position as they were housed in the triaxial system, i.e., flow entered the specimen from the bottom and exited from the top. Each specimen has one major wormhole, which has the largest diameter and connects the inlet and outlet. There are several secondary wormholes in each specimen, which developed at the inlet of the specimen near the major wormhole. Along the major and secondary wormholes, branches also developed presenting a root-like geometry (Daccord et al., 1993a). Figure 5 shows a generally accepted trend that as the flow rate increases, there are more secondary wormholes, and more branches on the wormholes (Daccord et al., 1993a; Fredd and Fogler, 1998; Budek and Szymczak, 2012). The surface area, volume and number of wormholes have been studied by Li et al., (2019), who showed that the wormholes only occupied a very small portion of the specimen volume. The ratio of wormhole volume to specimen volume is around 0.4% for the seven specimens.

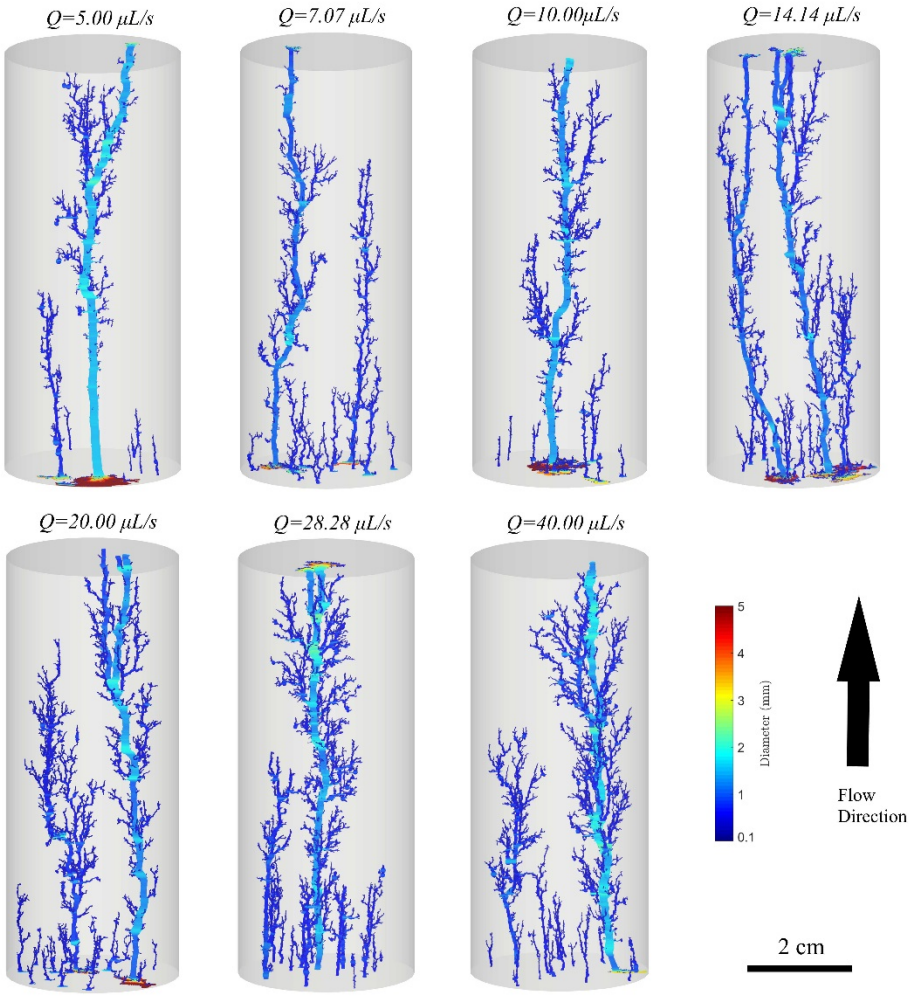

Figure 5. 3D reconstructions of the wormholes in each specimen. The wormhole geometries showed that higher flow rates resulted in more complicated wormholes.

4.2. Skeleton analysis

The complexity of the wormholes can be studied by analyzing their topological skeletons. The MATLAB built-in 3D skeletonization function "bwskel" was applied on the 3D binary matrices that represent the wormholes in each specimen. The skeletons extracted from the wormholes are shown in Figure 6. The skeletonization algorithm reduced the wormholes with tens of voxels in diameter to lines with a single voxel in diameter.

The total length of all the wormholes in each specimen can be calculated based on the skeletons of the wormholes. The skeletonization reduces the diameter of the wormholes to a single voxel, but preserves the lengths of the wormholes. Therefore, the lengths of the skeletons are the same as those of the wormholes. Since the skeleton only have a diameter of one voxel, the voxel length of the skeleton is the number of voxels representing the skeleton. The voxel length of the skeleton can be converted to meters using the scale factor of 50 μm/voxel. Thus, the lengths of the skeletons, which is also the lengths of the wormholes can be calculated. The lengths of the wormholes for each specimen is summarized in Figure 7.

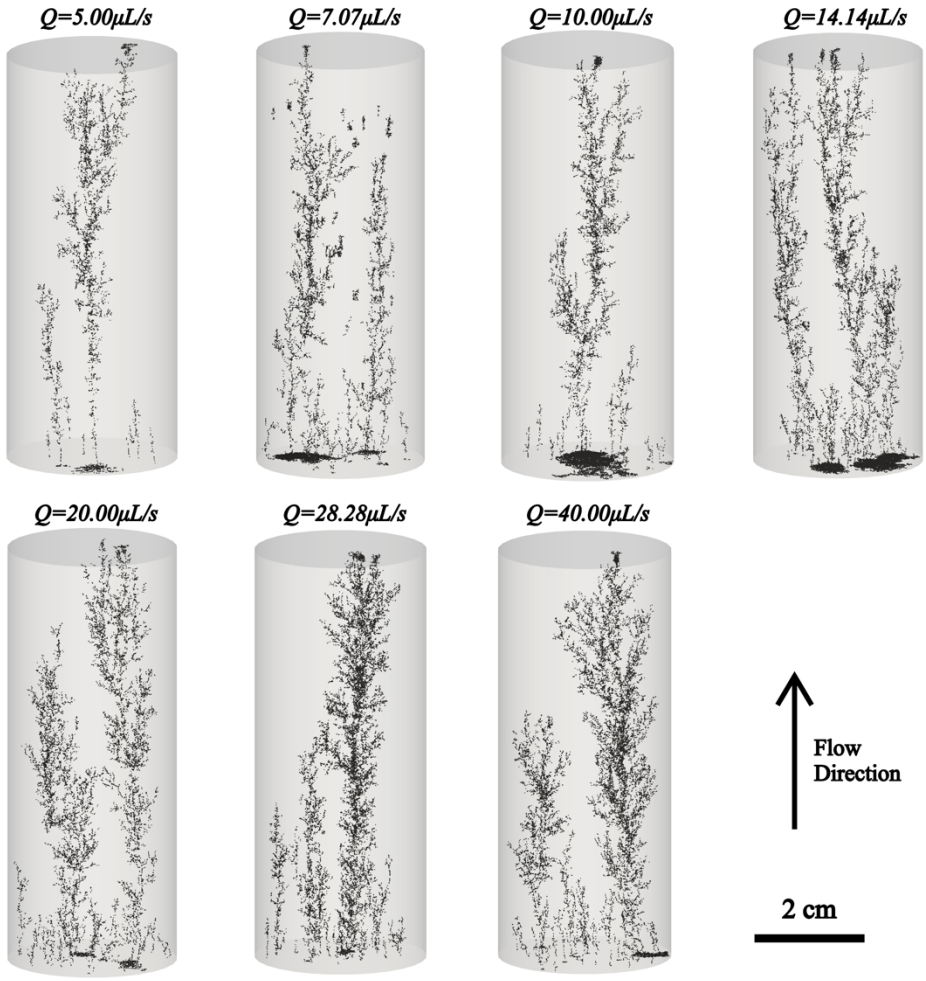

Figure 6. Wormhole skeletonization.

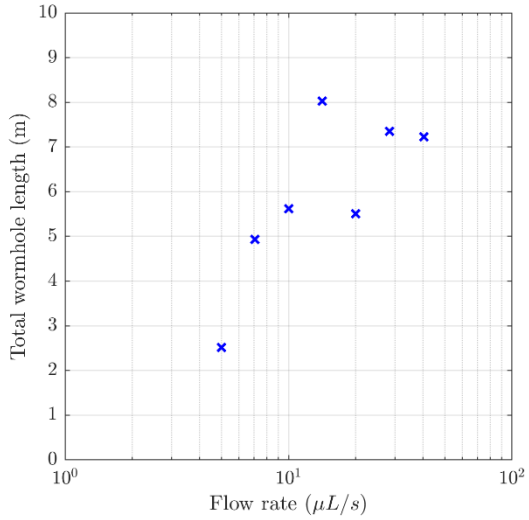

Figure 7. Total length of the wormholes in each specimen resulting from different flow rates.

As shown in Figure 7, the total lengths of the wormholes resulting from the different flow rates are at the scale of several meters, which are two orders of magnitude longer than the specimens (82.55 *mm*). Although the length of the major wormhole in each specimen is comparable to the specimen length, the complex branching and meandering of the wormholes result in much longer lengths, collectively. Figure 7 also shows that the wormholes resulting from higher flow rates tend to have longer length, except for the wormholes resulting from Q=14.14 *μL/s*. In the case of Q=14.14 *μL/s*, the wormholes are longer than the wormholes resulting from higher flow rates because there are two wormholes connecting the inlet and outlet. This is not a common case for wormhole formation. Clearly, if there are two or more wormholes developed independently and connect the inlet and outlet of the specimen, with their branches, the total length is expected to be longer.

4.3. Fractal analysis

The wormholes shown in Figure 5 exhibit a complex fractal pattern. To quantify the complex geometry of the wormholes and compare the wormholes resulting from different flow rates, the fractal dimension (D_f) is used. The fractal dimension is defined as the ratio providing a statistical index of complexity comparing how details in a pattern (strictly speaking, a fractal pattern) change with the scale at which they are measured. It has also been characterized as a measure of the space-filling capacity of

a pattern that indicates how a fractal scales differently in the space it is embedded in (Mandelbrot, 1982; Viscek, 1992; Sagan, 1994; Falconer, 2003). Higher fractal dimensions indicate more complex geometry. For a fractal geometric pattern in a 3D volume, D_f ranges from 1 to 3.

Since the wormholes are represented by a 3D binary matrix, the box counting method is used to characterize the fractal dimension of these wormholes. The box counting method uses boxes to characterize the details of a fractal pattern. The size of the box represents the scale of observation, while the number of boxes used to cover the fractal pattern represents the level of details. This method finds the relation between the size of the boxes (R_b) and the number of boxes of this size needed to cover the wormholes (N_b). The box scans through the 3D binary matrix with a fixed grid scan strategy, which moves the box the same distance as the size of the box. The results of the box counting of the seven specimens are shown in Figure 8.

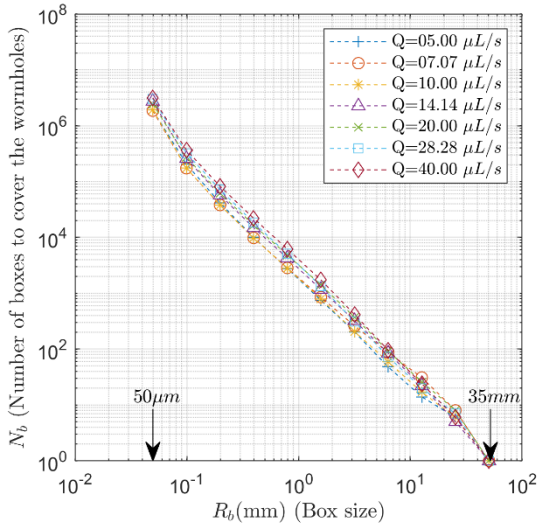

Figure 8. Relation between N_b and R_b using box counting method.

Figure 8 shows that the number of boxes needed to cover all the wormholes in a specimen decreases with the box size. The relatively similar positioning of the seven curves also indicates that the wormholes in the seven specimens show similar fractal feature. When the box size is 50 μm, which is the voxel size of the CT scan, N_b is the number of voxels representing the wormholes. When the box size is around 35mm, which is the diameter of the specimen, only one box is needed, as shown in Figure 8.

A linear fit was used to find the relation between $log(N_b)$ and $log(R_b)$, as shown in Figure 9. The wormholes resulting from the flow rate Q=5.00 $\mu L/s$ is used as an example. A reasonably good fit was obtained using the linear fit (Figure 9). According to the definition of fractal dimension, the slope of this fit is then the fractal dimension D_f,

$$D_f = -\frac{\Delta log N_b}{\Delta log R_b}. \quad (3)$$

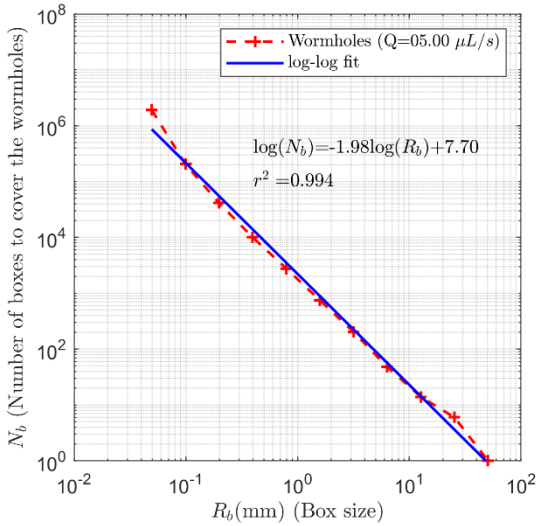

Figure 9. Linear fit between $log(N_b)$ and $log(R_b)$, The wormholes resulting from Q=5.00 $\mu L/s$ is used as an example.

As shown in Figure 9, the fractal dimension of the wormholes resulting from the flow rate Q=05.00 $\mu L/s$ is 1.98. The fractal dimension (D_f) and the y-intercepts (D_0) of the wormholes in the seven specimens are summarized and plotted in Figures 10(a) and (b). The wormholes of the seven specimens have a fractal dimension around 2. This is a relatively high fractal dimension given the wormholes have a tubular geometry and only occupy 0.4% of the total specimen volume, as discussed in Section 4.1. Although the wormholes have a small volume, they exhibit topological complexity similar to a two dimensional object. Figure 10 (a) also shows that the fractal dimensions are higher for wormholes resulting from higher flow rates. The wormhole complexity characterized by fractal dimensions matches the generally accepted conclusion that higher flow rate results in more complex wormholes (Daccord et al., 1993a; Fredd and Fogler, 1998; Budek and Szymczak, 2012).

Some researchers used numerical models to simulate the wormhole formation and study the fractal dimensions of the wormholes (Liu and Zhao, 2005; Kalia and Balakotaiah, 2007; Ming et al., 2012). However, these studies were limited to two-dimensional models and the fractal dimension calculated based on these simulations are in the range of 1.4-1.7. This study showed that the 3D wormholes resulting from the core flood tests have fractal dimensions higher than those resulting from numerical solutions. This analysis can be used as a reference for the numerical studies in the future.

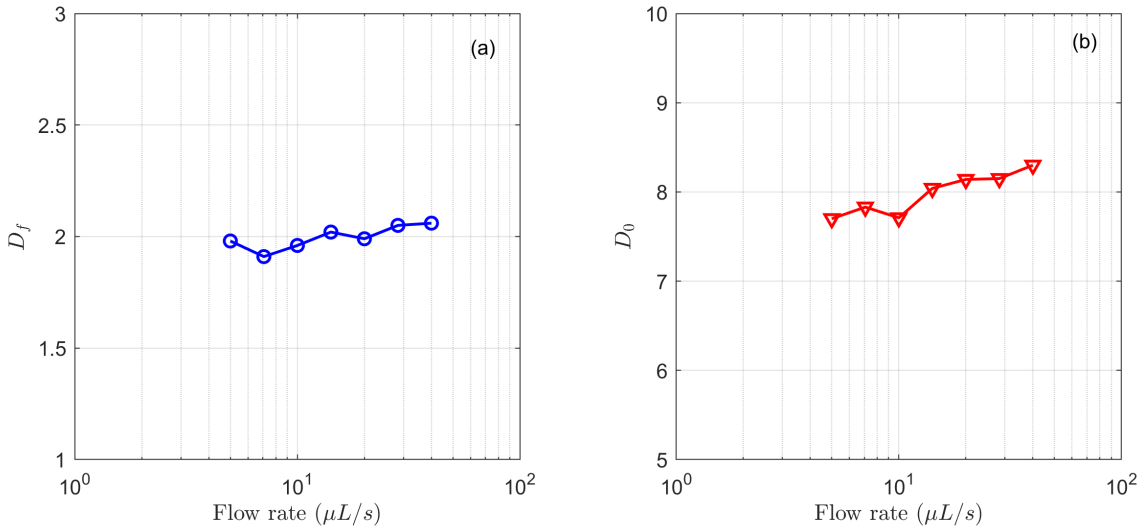

Figure 10. Fractal dimension (D_f) and y-intercepts (D_0) of the wormholes resulting from different flow rates. (a) Fractal dimension. (b) y-intercept.

The y-intercept in Figure 10(b) is a factor that depends not only on the wormhole geometry but also on the units used during the analysis. Since the units and analysis methods are consistent across the wormholes of the seven specimens, the relative value can thus be used to evaluate the complexity of the wormholes. In this case, a higher y-intercept indicates more boxes are needed to cover the wormholes, which again indicates higher complexity. As shown in Figure 10(b), the y-intercepts also show that higher flow rates indeed result in more complex wormholes.

5. SUMMARY AND CONCLUSIONS

Core flood tests were conducted to study the effect of flow rate on the formation of wormholes. The wormholes resulting from different flow rates were observed using high resolution X-ray CT scanning. Topological and morphological algorithms were developed to process the 3D CT scan data and reconstruct the geometry of wormholes in the specimens. Skeleton analysis was used to study the geometry of the wormhole regarding the total wormhole length. Fractal analysis was used to study the complexity of the wormhole geometry. These analyses provided quantitative descriptions of the complex wormholes and showed how the flow rates affect the geometry of wormholes.

More specifically, the total lengths of the wormholes in each specimen were calculated using skeleton analysis. The total length of the wormholes in each specimen is about two orders of magnitude longer than the specimen itself. Higher flow rates tend to result in wormholes that have longer total lengths. The wormholes in the specimen have fractal dimensions around 2 according to the fractal analysis of the 3D CT scan data. The fractal dimensions of wormholes resulting from higher flow rate is higher. Hence, the skeleton analysis and fractal analysis quantitatively and consistently showed that higher flow rates lead to more complex wormholes.

The skeleton analysis and fractal analysis not only confirmed the generally accepted conclusion that higher flow rates result in more complex wormholes, but also provided useful references for the studies of wormhole formation or underground flow network systems in general. As discussed in the skeleton analysis (Section 4.2), the total lengths of the wormholes could be as high as two orders of magnitude longer than the distance between the inlet and outlet. Although the wormholes are tubular shaped and only occupy a very small ratio of specimen volume (0.4%), they exhibit topological complexity similar to a two dimensional object with fractal dimensions around 2. These experimental results can be used as reference for future theoretical and numerical studies on wormhole formation.

ACKNOWLEDGEMENT

This work was partially funded by the Abu Dhabi National Oil Company and the Cooperative Agreement between the Masdar Institute of Science and Technology (Masdar Institute), Abu Dhabi, UAE and the Massachusetts Institute of Technology (MIT), Cambridge, MA, USA-Reference 02/MI/MIT/CP/11/07633/GEN/G/00. The authors also acknowledge the help in designing and fabricating the ECMS from Stephen W. Rudolph in the Department of Civil and Environmental Engineering at MIT. The authors also thank their colleagues Rafael Villamor Lora and Hao Kang for their help in updating and servicing the triaxial system.

REFERENCE

1. Abdulhadi, N. O., J. T. Germaine, and A. J. Whittle (2011), Thick-walled cylinder testing of clays for the study of wellbore instability, *Geotechnical Testing Journal*, *34*(6), 746–754.
2. Al-Khulaifi, Y., Q. Lin, M. J. Blunt, and B. Bijeljic (2018), Reservoir-condition pore-scale imaging of dolomite reaction with supercritical co2 acidified brine: Effect of pore-structure on reaction rate using velocity distribution analysis, *International Journal of Greenhouse Gas Control*, *68*, 99–111.
3. Andersen, G. R. (1991), Physical mechanisms controlling the strength and deformation behavior of frozen sand, Ph.D. thesis, Massachusetts Institute of Technology.
4. Budek, A., and P. Szymczak (2012), Network models of dissolution of porous media, *Physical Review E*, *86*(5), 056,318.
5. Cai, Z., H. Wen, S. Komarneni, and L. Li (2018), Mineralogy controls on reactive transport of marcellus shale waters, *Science of The Total Environment*, *630*, 1573–582.
6. Daccord, G. (1987), Chemical dissolution of a porous medium by a reactive fluid, *Physical review letters*, *58*(5), 479.
7. Daccord, G., and R. Lenormand (1987), Fractal patterns from chemical dissolution, *Nature*, *325*(6099), 41–43.
8. Daccord, G., R. Lenormand, and O. Lietard (1993a), Chemical dissolution of a porous medium by a reactive fluid –i. model for the "wormholing" phenomenon, *Chemical Engineering Science*, *48*(1), 169–178.
9. Daccord, G., O. Lietard, and R. Lenormand (1993b), Chemical dissolution of a porous medium by a reactive fluid –ii. convection vs reaction, behavior diagram, *Chemical engineering science*, *48*(1), 179–186.
10. Deng, H., J. P. Fitts, D. Crandall, D. McIntyre, and C. A. Peters (2015), Alterations of fractures in carbonate rocks by CO_2-acidified brines, *Environmental science & technology*, *49*(16), 10,226–10,234.
11. Deng, H., J. P. Fitts, and C. A. Peters (2016), Quantifying fracture geometry with x-ray tomography: Technique of iterative local thresholding (tilt) for 3d image segmentation, *Computational Geosciences*, *20*(1), 231–244.
12. Deng, H., M. Voltolini, S. Molins, C. Steefel, D. DePaolo, J. Ajo-Franklin, and L. Yang (2017), Alteration and erosion of rock matrix bordering a carbonate-rich shale fracture, *Environmental science & technology*, *51*(15), 8861–8868.
13. Einstein, H., R. Hirschfeld, R. Nelson, and R. Bruhn (1969), Model studies of jointed rock behavior, in *The 11th US Symposium on Rock Mechanics (USRMS)*, American Rock Mechanics Association.
14. El-Maghraby, R. M., and M. J. Blunt (2012), Residual co 2 trapping in Indiana limestone, *Environmental science & technology*, *47*(1), 227–233.
15. Falconer, K. (2004). Fractal geometry: mathematical foundations and applications. John Wiley & Sons.
Fredd, C. N., and H. S. Fogler (1998), Influence of transport and reaction on wormhole formation in porous media, *AIChE journal*, *44*(9), 1933–1949.
16. Ghommem, M., W. Zhao, S. Dyer, X. Qiu, and D. Brady (2015), Carbonate acidizing: modeling, analysis, and characterization of wormhole formation and propagation, *Journal of Petroleum Science and Engineering*, *131*, 18–33.
17. Gomaa, A. M., and H. A. Nasr-El-Din (2010), New insights into the viscosity of polymer-based in-situ-gelled acids, *SPE Production & Operations*, *25*(03), 367–375.
18. Gouze, P., C. Noiriel, C. Bruderer, D. Loggia, and R. Leprovost (2003), X-ray tomography characterization of fracture surfaces during dissolution, *Geophysical Research Letters*, *30*(5).
19. Hao, Y., M. Smith, Y. Sholokhova, and S. Carroll (2013), Co 2 -induced dissolution of low permeability carbonates. part ii: Numerical modeling of experiments, *Advances in water resources*, *62*, 388–408.
20. Hoefner, M., and H. S. Fogler (1988), Pore evolution and channel formation during flow and reaction in porous media, *AIChE Journal*, *34*(1), 45–54.
21. Kalia, N., and V. Balakotaiah (2007), Modeling and analysis of wormhole formation in reactive dissolution of carbonate rocks, *Chemical Engineering Science*, *62*(4), 919–928.
22. Li, W., H. H. Einstein, and J. T. Germaine (2019), An experimental study of matrix dissolution and wormhole formation using gypsum core flood tests. Part i: Permeability evolution and 3d wormhole reconstruction, *Journal of Geophysical Research: Solid Earth*, *xxx*(xx), xxxx–xxxx (In revision).
23. Lin, Q., Y. Al-Khulaifi, M. J. Blunt, and B. Bijeljic (2016), Quantification of subresolution porosity in carbonate rocks by applying high-salinity contrast brine using x-ray microtomography differential imaging, *Advances in water resources*, *96*, 306–322.
24. Liu, X., G. Zhao, et al. (2005), A fractal wormhole model for cold heavy oil production, *Journal of Canadian Petroleum Technology*, *44*(09).
25. Mandelbrot, B. B. (1982). The fractal geometry of nature (Vol. 2). New York: WH freeman.
26. Menke, H., M. Andrew, M. Blunt, and B. Bijeljic (2016), Reservoir condition imaging of reactive transport in heterogeneous carbonates using fast synchrotron tomography—effect of initial pore structure and flow conditions, *Chemical Geology*, *428*, 15–26.
27. Menke, H., C. Reynolds, M. Andrew, J. P. Nunes, B. Bijeljic, and M. Blunt (2018), 4D multi-scale imaging of reactive flow in carbonates: Assessing the impact of heterogeneity on dissolution regimes using streamlines at multiple length scales, *Chemical Geology*, *481*, 27–37.
28. Ming, L., S. Zhang, and M. Jianye (2012), Fractal nature of acid-etched wormholes and the influence of acid type on wormholes, *Petroleum Exploration and Development, 39*(5), 630–635.
29. Mohamed, I. M., J. He, and H. A. Nasr-El-Din (2013), Experimental analysis of CO_2 injection on

permeability of vuggy carbonate aquifers, *Journal of Energy Resources Technology*, *135*(1), 013,301.
30. Noiriel, C. (2015), Resolving time-dependent evolution of pore-scale structure, permeability and reactivity using x-ray microtomography, *Reviews in Mineralogy and Geochemistry*, *80*(1), 247–285.
31. Noiriel, C., and D. Daval (2017), Pore-scale geochemical reactivity associated with CO_2 storage: New frontiers at the fluid–solid interface, *Accounts of chemical research*, *50*(4), 759–768.
32. Noiriel, C., L. Luquot, B. Madé, L. Raimbault, P. Gouze, and J. Van Der Lee (2009), Changes in reactive surface area during limestone dissolution: An experimental and modelling study, *Chemical Geology*, *265*(1-2), 160–170.
33. No. 1 moulding plasters (Tech. Rep. No. SDS NO. 52000000006). (2017, 3). 550 West Adams Street, Chicago, Illinois, 60661: United States Gypsum Company. (Version #: 3)
34.
35. Reynolds, C., M. Blunt, and S. Krevor (2014), Impact of reservoir conditions on CO_2-brine relative permeability in sandstones, *Energy Procedia*, *63*, 5577–5585.
36. Sagan, H. (2012). Space-filling curves. Springer Science & Business Media.
37. Sayed, M. A. I., A. S. E. D. Zakaria, H. A. Nasr-El-Din, S. P. Holt, H. Almalki, et al. (2012), Core flood study of a new emulsified acid with reservoir cores, in *SPE International Production and Operations Conference & Exhibition*, Society of Petroleum Engineers.
38. Serafeimidis, K., and G. Anagnostou (2013), On the time-development of sulphate hydration in anhydritic swelling rocks, *Rock mechanics and rock engineering*, *46*(3), 619–634.
39. Sheahan, T. C., and J. T. Germaine (1992), Computer automation of conventional triaxial equipment, *Geotechnical Testing Journal*, *15*(4), 311–322.
40. Smith, M. M., Y. Sholokhova, Y. Hao, and S. A. Carroll (2013), Co 2 -induced dissolution of low permeability carbonates. part i: Characterization and experiments, *Advances in Water Resources*, *62*, 370–387.
41. Smith, M. M., Y. Hao, H. E. Mason, and S. A. Carroll (2014), Experiments and modeling of variably permeable carbonate reservoir samples in contact with CO_2-acidified brines, *Energy Procedia*, *63*(C).
42. Smith, M. M., Y. Hao, and S. Carroll (2017), Development and calibration of a reactive transport model for carbonate reservoir porosity and permeability changes based on CO_2 core-flood experiments, *International Journal of Greenhouse Gas Control*, *57*, 73–88.
43. Su, I., Z. Qin, T. Saraceno, A. Krell, R. Mühlethaler, A. Bisshop, and M. J. Buehler (2018), Imaging and analysis of a three-dimensional spider web architecture, *Journal of The Royal Society Interface*, *15*(146), 20180,193.
44. Taylor, K., and H. Nasr-El-Din (2002), Coreflood evaluation of in-situ gelled acids, in *International Symposium and Exhibition on Formation Damage Control*, Society of Petroleum Engineers.
45. Vicsek, T. (1992). Fractal growth phenomena. World scientific.
46. Wang, H., Y. Bernabé, U. Mok, and B. Evans (2016), Localized reactive flow in carbonate rocks: Core-flood experiments and network simulations, *Journal of Geophysical Research: Solid Earth*, *121*(11), 7965–7983.